Effect of mechanical alloying and spark plasma sintering on the microstructure and mechanical properties of ODS Eurofer

Fu, J.; Brouwer, J. C.; Richardson, I. M.; Hermans, M. J.M.

DOI
10.1016/j.matdes.2019.107849

Publication date
2019

Document Version
Final published version

Published in
Materials and Design

Materials and Design 177 (2019) 107849

Contents lists available at ScienceDirect

Materials and Design

journal homepage: www.elsevier.com/locate/matdes

Effect of mechanical alloying and spark plasma sintering on the microstructure and mechanical properties of ODS Eurofer

J. Fu *, J.C. Brouwer, I.M. Richardson, M.J.M. Hermans

Department of Materials Science and Engineering, Delft University of Technology, Delft, the Netherlands

HIGHLIGHTS

- This is the first detailed report on the fabrication of ODS Eurofer via mechanical alloying and spark plasma sintering.
- The optimal fabrication conditions are determined.
- Bimodal microstructure, carbides and Y_2O_3 contribute to the mechanical properties of the bulk steel.
- Spark plasma sintering is proved to be a promising consolidation technique to fabricate high performance ODS Eurofer.

GRAPHICAL ABSTRACT

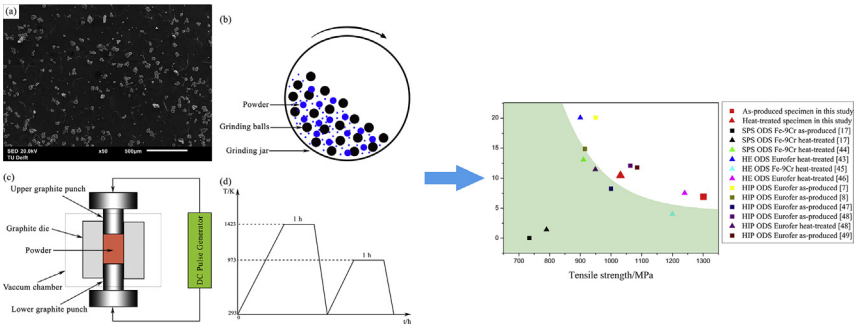

ARTICLE INFO

Article history:
Received 18 March 2019
Received in revised form 6 May 2019
Accepted 11 May 2019
Available online 14 May 2019

Keywords:
Oxide dispersion strengthened steel
Powder metallurgy
Spark plasma sintering
Microstructure
Mechanical properties

ABSTRACT

Oxide dispersion strengthened (ODS) Eurofer steel was prepared via mechanical alloying (MA) and spark plasma sintering (SPS). Different combinations of MA and SPS parameters were adopted in order to optimise the fabrication process. The experimental results show that the sample milled for 30 h, sintered at 1373 K at a pressure of 60 MPa has the highest density and microhardness among all the results obtained. As-produced ODS Eurofer shows a bimodal microstructure with homogeneously dispersed nanoscale Y_2O_3, that is beneficial for the mechanical properties. The yield and tensile strengths are higher while the elongation is lower in the top and bottom surfaces compared to the middle area of the sample. This is due to the presence of a larger number of $M_{23}C_6$ carbides, resulting from carbon diffusion from the mould material. As-produced samples were also subjected to a heat treatment. A good balance is achieved between the strength and ductility of the heat-treated material. Yielding properties comparable to hot isostatic pressing or hot extrusion as reported in the literature, the processing route presented by this study shows potential to produce high performance ODS Eurofer.

1. Introduction

Oxide dispersion strengthened (ODS) reduced activation ferritic/martensitic (RAFM) steels are promising candidates to be employed as high-performance structural materials for advanced fusion and fission reactors [1–6]. Within the European Union, ODS steels research has been focused on ODS Eurofer (9% CrWVTa) [4], which is based on European RAFM reference steel Eurofer 97 reinforced with 0.3 wt% Y_2O_3 nanoparticles. Compared to Eurofer 97, ODS Eurofer shows a pronounced increase in tensile strength, yield strength and creep strength from room temperature to high temperature up to 973 K [7,8]. This behaviour is mainly attributed to the presence of the highly dispersed and extremely stable Y_2O_3 particles, which act as obstacles

* Corresponding author.
E-mail address: j.fu@tudelft.nl (J. Fu).

https://doi.org/10.1016/j.matdes.2019.107849

Table 1
Chemical composition of ODS Eurofer and the powder size used in this study.

	Cr	W	Mn	V	Ta	Y_2O_3	Fe
wt./%	9.0	1.1	0.4	0.2	0.12	0.3	Bal.
Size/μm	38–45	45–75	45–115	Max 45	Max 75	0.025–0.05	Max 60

for the movement of dislocations and trapping sites for point defects induced by radiation displacement [9,10].

A powder metallurgy route is generally applied to produce ODS steels, involving mechanical alloying (MA), consolidation techniques and thermal/mechanical treatments. Hot isostatic pressing (HIP) or hot extrusion (HE) are commonly used to consolidate the mechanical alloyed powders. However, anisotropic and textured grains and relatively high costs due to long hold times are issues to be considered [11,12]. Therefore, an alternative and more cost-effective consolidation method is currently being explored. Spark Plasma Sintering (SPS), also known as Pulsed Electric Current Sintering (PECS) or Field Assisted Sintering Technology (FAST), is a sintering technique employing a pulsed direct electrical current and uniaxial pressure simultaneously to perform high speed consolidation of the powder [13]. This facilitates a very high heating (up to 2000 K/ min) and cooling rates (up to 150 K/ min), hence enhancing densification over grain growth, leading to a fully dense product with minimum grain growth [14]. SPS offers many advantages over conventional consolidation techniques such as HIP and HE, including short processing time, ease of operation and the ability to control any stage of sintering [15,16].

In recent years, MA and SPS have been employed to produce different types of ODS steels, however the application on ODS RAFM steels, especially ODS Eurofer is very limited. Sun et al. [17] has fabricated Fe-9Cr-1.5W-0.45Mn-0.1Ta-0.2V-0.01Si-0.2Ti-0.3Y_2O_3-0.1/0.2C (wt%) steels by MA and SPS. Chemical reduction was used to synthesise Fe-0.3Y_2O_3 powders. The tensile properties of the as-produced and annealed samples were studied. Poor elongations were obtained after tensile testing, indicating brittle fractures. Xie et al. [18] reported the grain morphology and nano-particles characterisation of Fe-9Cr-1.5W-0.4Mn-0.2V-0.1Ta-0.3Ti-0.3Y_2O_3 (wt%) prepared by MA and SPS. By proposing a yield strength model considering the contributions of solid solutes, grain size and nanoparticles, dispersion strengthening of $Y_2Ti_2O_7$ nanoparticles was found to be the major strengthen mechanism in the material. Ukai [19] investigated the phase transformation and the mechanical response of Fe-9Cr-2W-0.2Ti-0.35Y_2O_3-0.13C (wt%) steel produced by MA and SPS. However, process optimisation was lacking in this study. To sum up, limited information is available in the literature concerning the microstructural evolution and mechanical behaviour of ODS Eurofer, in particular their relationship with processing conditions.

The aim of this study is to assess the potential of MA and SPS to fabricate ODS Eurofer engineered for high strength combined with reasonable ductility. Opening a new window for the fabrication of ODS Eurofer, the study will contribute to the application of this material in nuclear reactors. Steel powders were milled and consolidated under various conditions. In addition, a number of samples were subjected to annealing and tempering treatments. Processing parameters were optimised based on the effect on the microstructure and mechanical properties. The results show that SPS in combination with MA are very promising techniques to produce ODS Eurofer with good properties.

Table 2
Processing conditions used in this study.

	Milling time/h	Pressure/MPa	Heating rate/(K/min)	Sintering temperature/K
A	0	50	100	1373
B	24	50	100	1373
C	30	50	100	1373
D	36	50	100	1373
E	30	40	100	1373
F	30	60	100	1373
G	30	80	100	1373
H	30	60	50	1373
I	30	60	200	1373
J	30	60	400	1373
K	30	60	100	1323
L	30	60	100	1423

2. Experimental details

2.1. Materials and preparation

The powders used in this study were commercially available Cr, W, Mn, V, Ta, Y_2O_3 and Fe powders, supplied by Goodfellow, Germany. All of them were weighted according to the nominal composition of ODS Eurofer indicated in Table 1. This table also shows the particle size of the powders provided by the manufacturer. Mechanically alloying was conducted in a Retsch planetary ball mill in an argon atmosphere using hardened steel balls (5 mm diameter) in a hardened steel bowl. The powders were milled for 6–36 h at a speed of 300 rpm with a ball to powder mass ratio of 3.4:1. These milling conditions were selected based on the study of Suryanarayana [20] on mechanical alloying and milling.

The as-milled powders were then compacted in a Spark Plasma Sintering (SPS, FCT group, Germany) machine under vacuum in a graphite die and graphite punches. Boron nitride spray was used inside the mould chamber to reduce carbon diffusion into the sample. The SPS compacts were heated at a heating rate of 50 to 400 K/ min up to the sintering temperature, which was chosen as 1323 K, 1373 K and 1423 K. The holding time at maximum temperature was 30 min. An axial pressure between 50 and 80 MPa was applied throughout the heating stage. The processing conditions used in the study are summarised in Table 2. Finally, the compacts were allowed to cool down to room temperature by direct contact with the water cooled punches. Following this procedure, disks with a diameter of 40 mm and a thickness of approximately 10 mm were produced. The final heat treatment was conducted on the disks to restore ductility by annealing at 1423 K for 1 h, air cooling to room temperature and then tempering at 973 K for 1 h, followed by air cooling to room temperature.

2.2. Analysis methods

The powders with different milling time were mounted and ground to obtain a flat surface. The as-produced specimens were prepared for microstructure characterisation by cutting across the centre of the

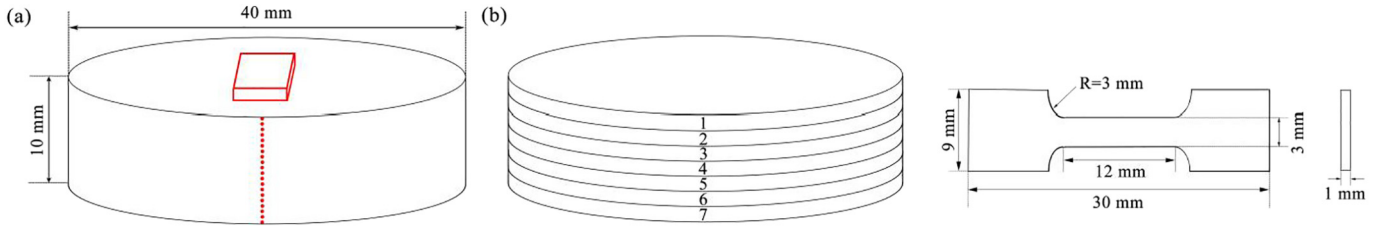

Fig. 1. (a) The position of the microstructure characterisation and hardness measurements. (b) The position, shape and dimensions of tensile samples.

sample, as indicated in Fig. 1(a). The surfaces of the specimens were mirror polished after grinding off the adherent graphite. The steels were then etched with Kalling's 1 reagent (2 g $CuCl_2$, 40 ml HCl, 40 ml ethanol and 40 ml water) for 30 s. The morphology of the powder and bulk steel were observed using JSM-6500F field emission scanning electron microscopy (SEM), equipped with an energy dispersive spectrometer (EDS). The content of carbon was determined with the carbon sulfur analyser (LECO CS744).

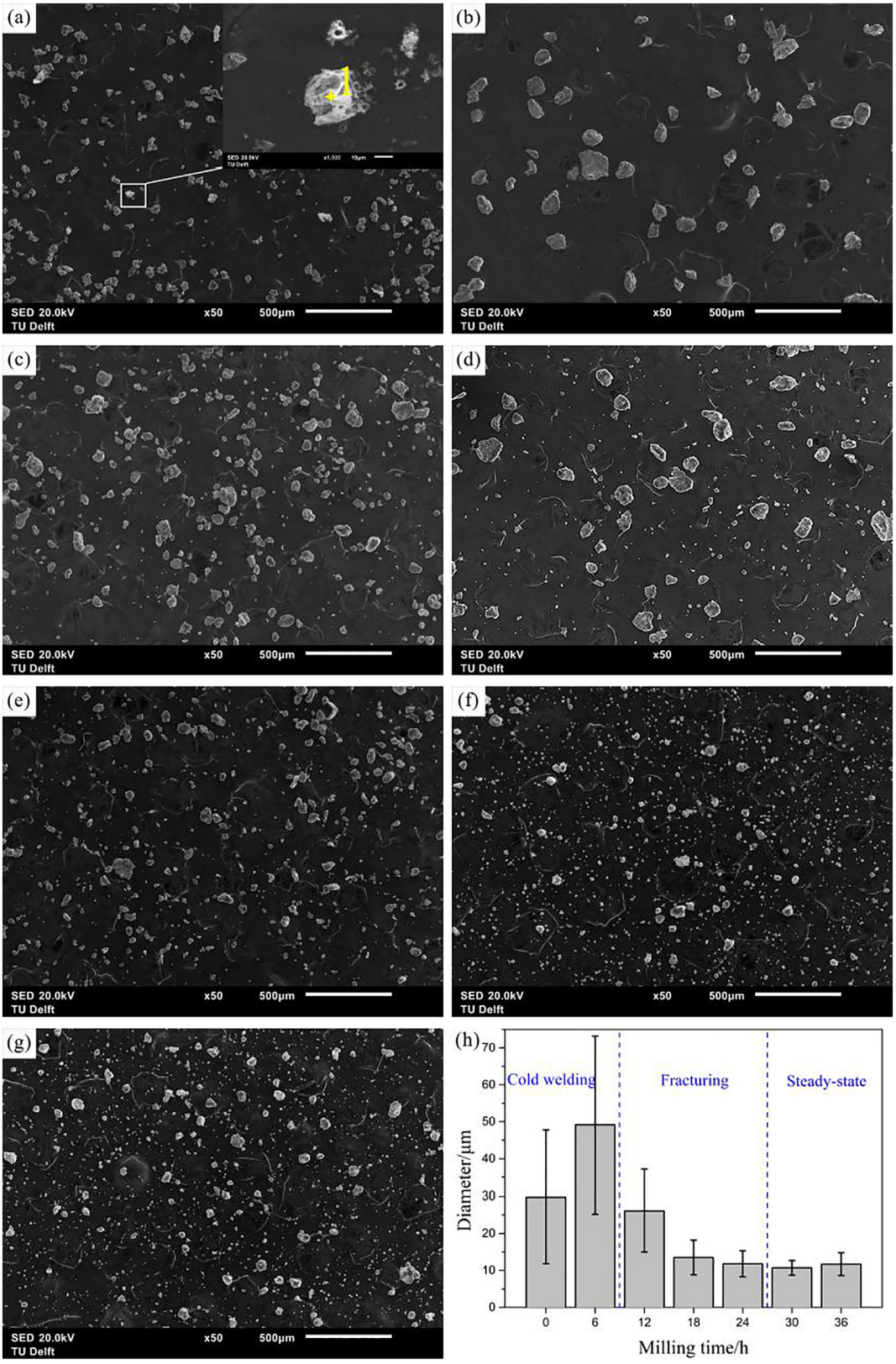

Fig. 2. SEM micrographs of (a) the as-mixed powders and the powders milled for (b) 6 h, (c) 12 h, (d) 18 h, (e) 24 h, (f) 30 h, (g) 36 h and (h) the variation of the powder size as a function of milling time.

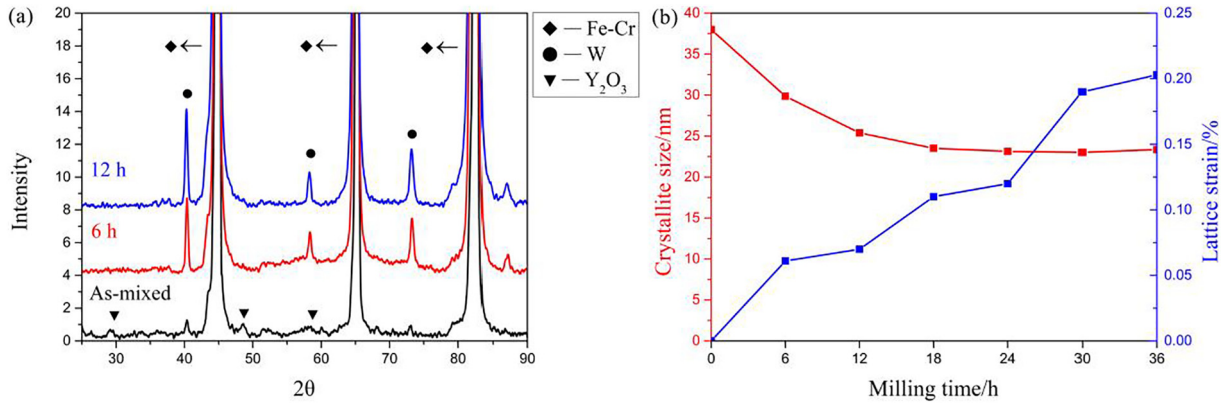

Fig. 3. (a) XRD patterns for mechanical alloyed powders. (b) Crystallite size and lattice strain as a function of milling time.

X-Ray diffraction (XRD) was performed using a Bruker D8 Advanced diffractometer with Cu Kα target (1.5406 Å) with a voltage of 45 kV and a current of 40 mA. A step size of 0.03° and a measuring time of 2 s per step were employed. LaB6 powder was used for the determination of the instrumental contributions to the peak width. The crystallite size D and lattice strain ε of the powders after mechanical alloying were calculated by Williamson-Hall equation [21]:

$$\beta cos\theta = \frac{K\lambda}{D} + 4\varepsilon sin\theta, \tag{1}$$

where β is the full width at the half maximum height (FWHM), θ is the Bragg angle, K is the Scherrer constant taken as 0.9 [22], λ is the X-Ray wavelength, D is crystallite size and ε is the lattice strain.

2.3. Property tests

The density of the consolidated samples was measured by the Archimedes method using the following equation:

$$\rho = \frac{m}{m - m_1}\rho_w, \tag{2}$$

where ρ is the density of the sample, m is the weight of the sample in air, m_1 is the weight of the sample in distilled water and ρ_w is the density of distilled water.

Vickers hardness measurements were performed under a load of 0.3 kg and repeated at least five times on the ground and polished surface while with a step size of 0.5 mm along the cross section (Fig. 1(a)). The specimens for tensile test were machined by wire electrical discharge machining (WEDM) according to Fig. 1(b). Specimens cut from the top to bottom were labelled from 1 to 7. Tensile test was conducted at a nominal strain rate of 2.5×10^{-4} s^{-1} at room temperature. The measurement was repeated for three times for each condition to verify the reproducibility of the results.

3. Results and discussion

3.1. Effect of mechanical alloying time

Fig. 2 presents the morphology and average size of the powders with different milling time investigated by SEM. It can be seen that the initial powders have a spherical shape (Fig. 2(a)), while the particles after the ball milling show irregular shapes due to severe amount of deformation applied (Fig. 2(b)–(g)). Fig. 2(h) summarizes the variation of the powder size as a function of milling time. The whole milling process can be divided into three stages: cold welding, fracturing and a steady-state stage [23]. In the cold welding stage (0–6 h), as the particles were relatively soft, they tend to weld together and generate large particles. This is the reason that the average diameter of the particles is increased after milling for 6 h compared to the as-mixed powders. The particle size distribution at this stage is wide, with some particles three to five times larger than the initial size. After that, in the fracturing stage (12–18 h), the powders were fragmented by intense collision and the mean size of the particles was decreased significantly. Finally, in the steady-state stage (24–36 h), it can be seen that the morphology and mean size of the powders show no significant change. This indicates that a dynamic equilibrium is attained where a balance between the rate of welding and fracturing is achieved. A narrow range of particle sizes develops at this stage, as the particles smaller than the mean size are agglomerated with about the same rate as the particles larger than the mean size are reduced. The average size of the particles reaches a minimum of 10.7 ± 2.0 μm after milling for 30 h. After a milling time of 36 h, a slight raise in the particles size up to 11.7 μm can be seen, which may be caused by the agglomeration of the small sized particles.

The XRD patterns of the mechanical alloyed powders are shown in Fig. 3(a). Fe—Cr mixture and W diffraction peaks can be clearly observed. Some peaks corresponding to yttria are observed in the case of the as-mixed powders due to yttria particle clusters. For instance, a yttria cluster of around 20 μm is identified by EDS, shown in Fig. 2(a). It is worth noticing that all of the yttria peaks are invisible when the powders have been milled for 6 h. This is probably ascribed to the reduction of the yttria particle size during the mechanical alloying process [24]. The absence of the yttria peaks also indicates that they have been incorporated into the steel matrix. Moreover, peak broadening with increasing milling time can be observed from the spectrum, ascribed to the decrease in the crystallite size and the increase in the lattice strain according to Eq. (1). The crystallite size and lattice strain estimated from the spectrum are shown in Fig. 3

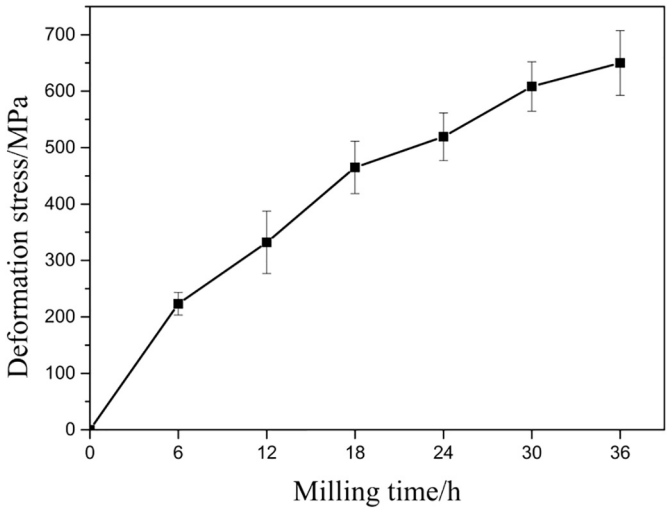

Fig. 4. Deformation stress as a function of milling time.

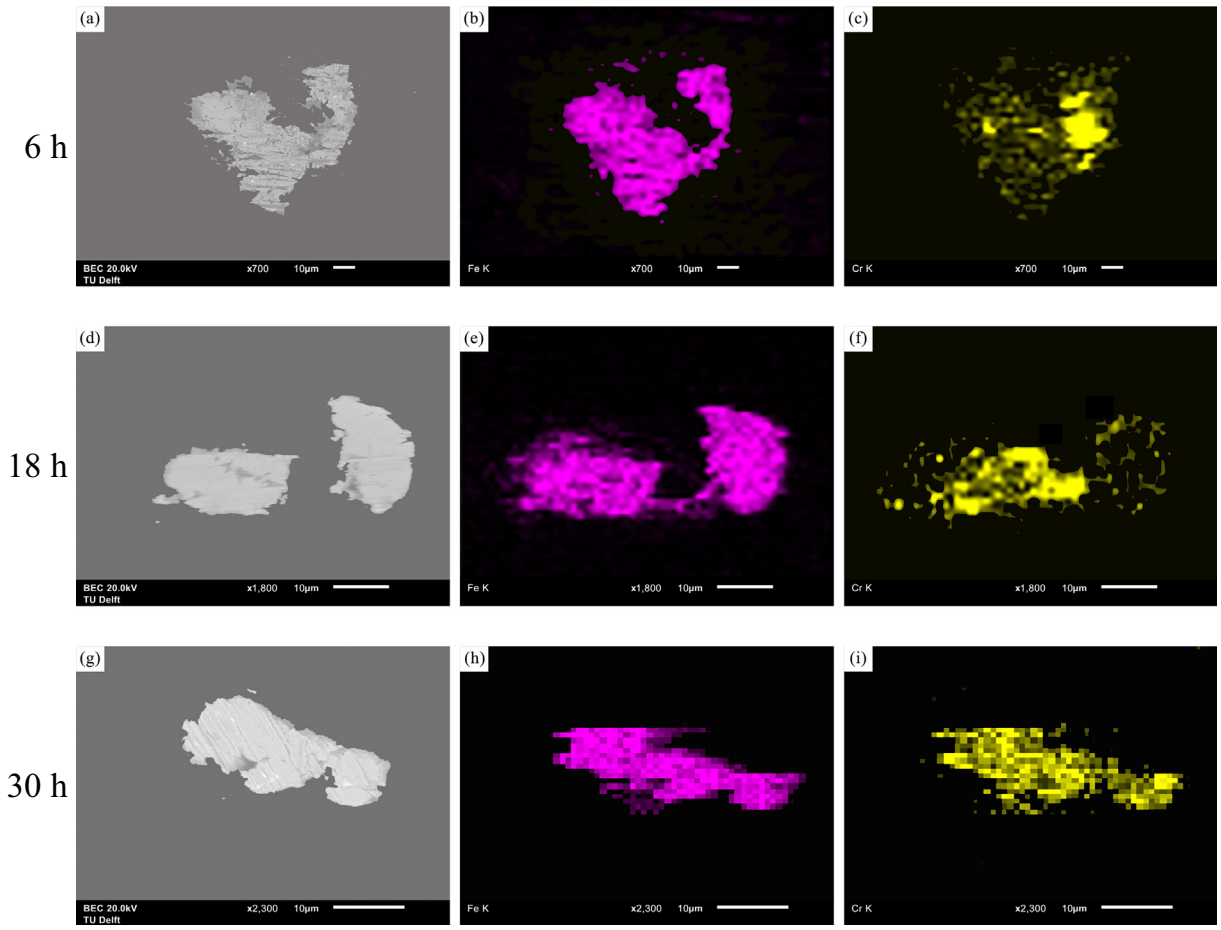

Fig. 5. EDS map scanning result of cross section of one powder particle milled for 6, 18 and 30 h. (a), (d) and (g) backscattered electron image; (b), (e) and (h) distribution map of Fe; (c), (f) and (i) distribution map of Cr.

(b). By increasing the milling time to 24 h, the crystallite size is decreased from 38 nm to 23 nm showing an obvious refinement effect, after which, it does not change significantly. Meanwhile, the lattice strain is increased to 0.2% when the milling time is increased to 36 h, which indicates that the dislocation density in the particles has been increased remarkably due to mechanical alloying.

A uniform stress deformation model (USDM) is used in order to estimate the deformation stress introduced by mechanical alloying [25]. In the USDM, the lattice deformation is assumed to be uniform in all the crystallographic directions. According to Hooke's law, $\sigma = E_{hkl}\varepsilon$, where σ is the stress of the crystal and E_{hkl} is Young's modulus in the [hkl] direction. By using this approach, the Williamson-Hall equation is now modified to

$$\beta cos\theta = \frac{K\lambda}{D} + \frac{4\sigma sin\theta}{E_{hkl}}. \tag{3}$$

E_{hkl} is given by

$$\frac{1}{E_{hkl}} = S_{11} - 2\left[(S_{11} - S_{12}) - \frac{1}{2}S_{44}\right]\left(\alpha^2\beta^2 + \alpha^2\gamma^2 + \beta^2\gamma^2\right), \tag{4}$$

where S_{11}, S_{12} and S_{44} are components of the compliance tensor and their estimated values for iron are 7.57×10^{-12}, -2.8×10^{-12} and 8.6×10^{-12} Pa^{-1}, respectively [26]. α, β, and γ are the direction cosines of the [hkl] direction and the [100], [010], and [001] directions, respectively.

The deformation stress of the ball milled powders is estimated using Eq. (3) and presented in Fig. 4. It can be clearly seen that the deformation stress increases with the milling time. The stress within the particles accumulates because of the intense collision between the powders and balls. The increasing deformation stress indicates that the powders were refined continuously during the intensive milling process.

Fig. 5 shows the EDS map scanning results of single particles taken from batches milled for 6 h, 18 h and 30 h. Only Fe and Cr are presented here as they account for approximately 98% of the ingredients of ODS Eurofer and therefore would be representative of the elemental distribution in the material. From the results, it can be observed that Fe and Cr started to mix after milling for 6 h (Fig. 5(a)–(c)). However, the chemical composition presented in Table 3 indicates a large deviation from the intended composition as listed in Table 1, although it should be emphasised that the presented composition is based on the characterisation of a single powder particle. After milling for 18 h, although

Table 3
Chemical composition of one powder particle for 6, 18 and 30 h obtained from EDS.

Elements (wt./%)	Cr	W	Mn	Y	V	Ta	Fe
6 h	2.56 ± 0.22	1.55 ± 0.23	0.72 ± 0.18	0.79 ± 0.18	0.28 ± 0.09	–	Bal.
18 h	6.75 ± 0.37	1.24 ± 0.36	0.54 ± 0.28	0.37 ± 0.28	0.26 ± 0.14	1.40 ± 1.40	Bal.
30 h	8.54 ± 0.25	1.05 ± 0.20	0.37 ± 0.19	0.22 ± 0.16	0.20 ± 0.09	0.89 ± 0.89	Bal.

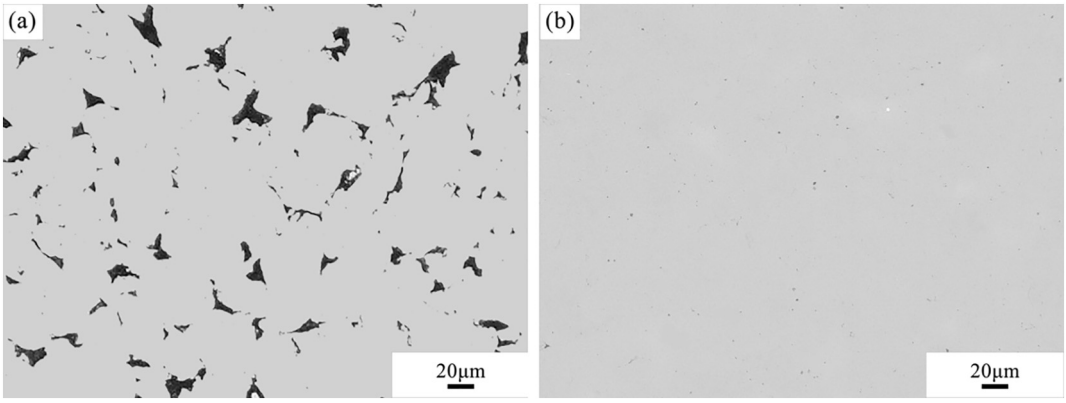

Fig. 6. Optical micrographs of SPS prepared samples (a) milled 30 h SPS at 1323 K (b) milled 30 h SPS at 1373 K.

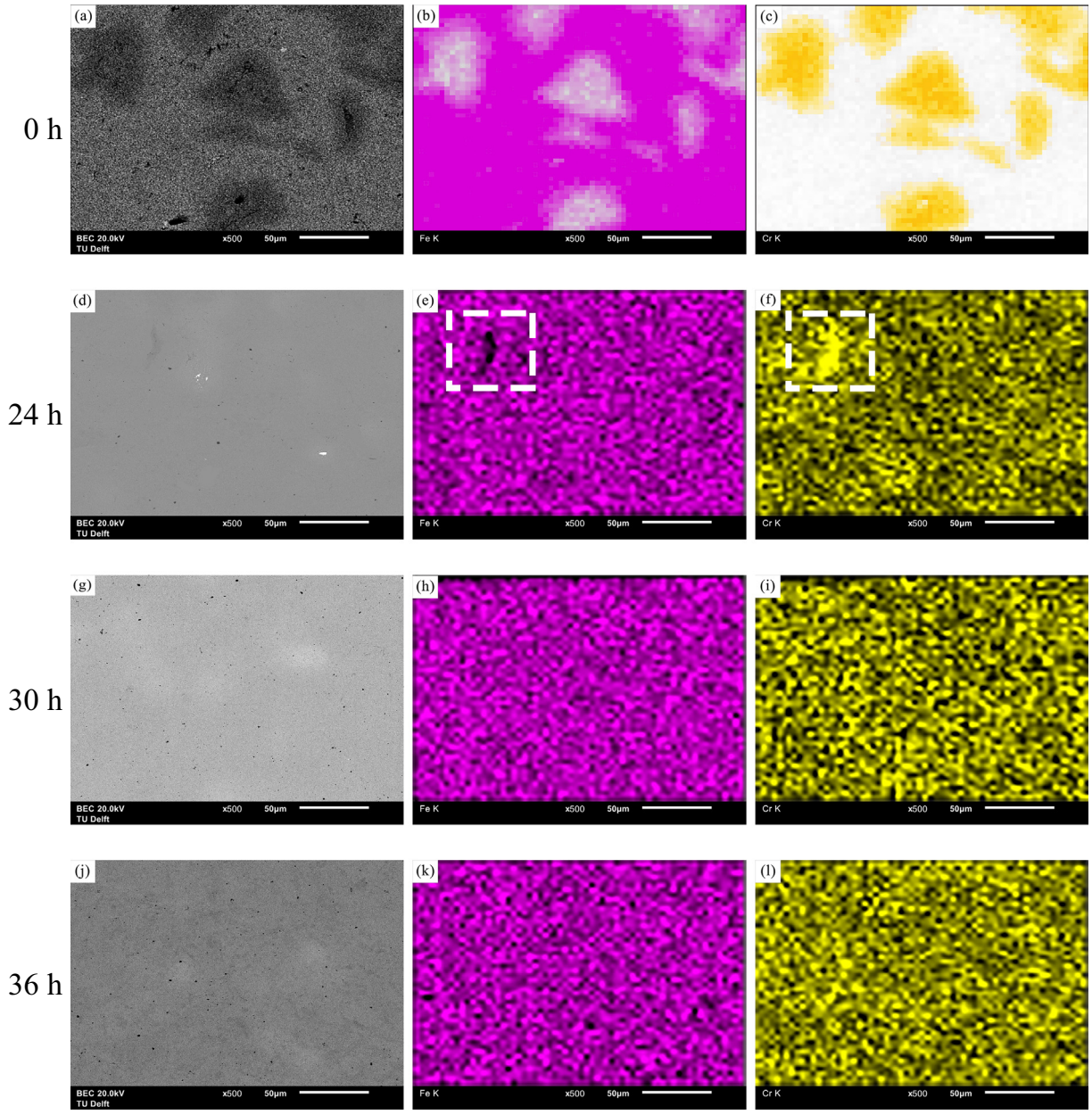

Fig. 7. EDS map scanning result of the sample produced by milling for 0 h, 24 h, 30 h and 36 h and SPS at 1373 K. (a), (d), (g) and (j) backscattered electron image; (b), (e), (h) and (k) distribution map of Fe; (c), (f), (i) and (l) distribution map of Cr. The inserted dashed rectangulars indicate uneven distributions of elements.

Table 4
Chemical composition of the sample produced by milling for 0 h, 24 h, 30 h and 36 h and SPS at 1373 K obtained from EDS.

Elements (wt./%)	Cr	W	Mn	Y	V	Ta	Fe
0 h	32.24 ± 0.82	0.28 ± 0.10	0.65 ± 0.10	0.13 ± 0.08	0.02 ± 0.02	0.49 ± 0.06	Bal.
24 h	9.96 ± 0.16	0.92 ± 0.11	0.46 ± 0.11	0.28 ± 0.08	0.15 ± 0.05	–	Bal.
30 h	9.19 ± 0.16	1.11 ± 0.17	0.33 ± 0.12	0.19 ± 0.09	0.20 ± 0.05	0.16 ± 0.16	Bal.
36 h	8.72 ± 0.16	1.18 ± 0.11	0.72 ± 0.12	0.29 ± 0.08	0.24 ± 0.05	0.18 ± 0.18	Bal.

the deviation of the chemical composition has been partially eliminated, Fe and Cr still did not mix very well. For instance, the left-hand side of the particle is rich in Cr, while the right-hand side shows the absence of Cr (Fig. 5(d)–(f)). After milling for 30 h, it seems that Fe and Cr were homogenously distributed in the powder due to repeated welding and fracturing (Fig. 5(g)–(i)). The chemical composition is very close to the intended composition, showing a sufficient mixing.

In conclusion, the effect of mechanical alloying is not only refinement of the (grain) size of the powders and introduction of high deformation stresses and a high dislocation density, but also the homogenous incorporation of the alloying elements into the steel matrix [27]. Considering the above findings, we can conclude that milling for at least 24 h is required to obtain refined powders with a homogeneously distributed composition, which is favourable for the following SPS process.

3.2. Effect of spark plasma sintering

Based on the previous results, the powders milled for 24 h, 30 h and 36 h were chosen as the raw material for SPS to produce bulk steels. An SPS prepared specimen using the as-mixed powders was used as a reference. The temperature of SPS is the first parameter to be determined because it is crucial for the efficiency of the sintering process. Taking the powders milled for 30 h as an example (sample K in Table 2), at sintering temperature of 1323 K (with a heating rate of 100 K/min and a pressure of 60 MPa), large pores in the microstructure are visible (Fig. 6(a)) suggesting limited sintering. When the sintering temperature was increased to 1373 K (sample F in Table 2), almost all pores were eliminated indicating the powders were sintered more efficiently (Fig. 6(b)). It is worth mentioning that local melting occurred when the temperature was increased to 1423 K (sample L in Table 2), revealing that the maximum applicable process temperature was exceeded. Thus, it appears that 1373 K is a suitable sintering temperature for the SPS process.

The EDS mapping results of the SPS prepared samples (sintered at 1373 K) are shown in Fig. 7. It can be clearly seen that without ball milling, Fe and Cr were non-uniformly distributed due to lack of mixing of the powders (Fig. 7(a)–(c)). Large cavities can be seen in the microstructure due to the size difference of the initial powders. Table 4 gives the information of the chemical composition. The chromium content of the scanned area (180 × 240 μm) is 32.24%, which is significantly higher than that of the as-mixed powders (Table 1). After 24 h of milling, some of the powders mixed together, but there were still uneven distributions in some areas as indicated in the white frames in Fig. 7 (e) and (f). A small deviation of the chemical composition from the intended average composition still exists, showing insufficient mixing. After 30 h and 36 h of milling, Fe and Cr mixed well and became homogeneously distributed (Fig. 7(g)–(l)). Moreover, in both cases, the chemical compositions of the scanned areas are in good agreement with that of the as-mixed powders. Therefore, a conclusion can be drawn that a sufficient and efficient mechanical alloying is of great importance to accomplish homogeneous and consistent chemical composition of ODS Eurofer, which is crucial to ensure the reproducibility considering its industrial application.

The milled powders were sintered at different pressures combined with different heating rates as indicated in Table 2. We evaluated the density and microhardness of the bulk steel in order to find the optimal processing parameters to produce the bulk steel with the best properties. Fig. 8 presents the density and surface hardness of the samples (sintered at 1373 K) under different processing conditions. It can be seen that the hardness of the fine grained area is higher than that of the coarse grained area. This bimodal microstructure feature will be addressed in the next section. From A, B, C and D, one can observe that the sample milled for 30 h (sample C) has the highest density and hardness. This can be attributed to two reasons; on the one hand, compared to the samples milled for 0 h and 24 h, the powders were distributed more homogenously and Y_2O_3 was introduced into the matrix of the base powder after sufficient ball milling, resulting in a harder material. On the other hand, the average size of the powders milled for 30 h is finest compared to the other conditions. This will cause the generation of fewer and smaller pores between the powders or grain boundaries.

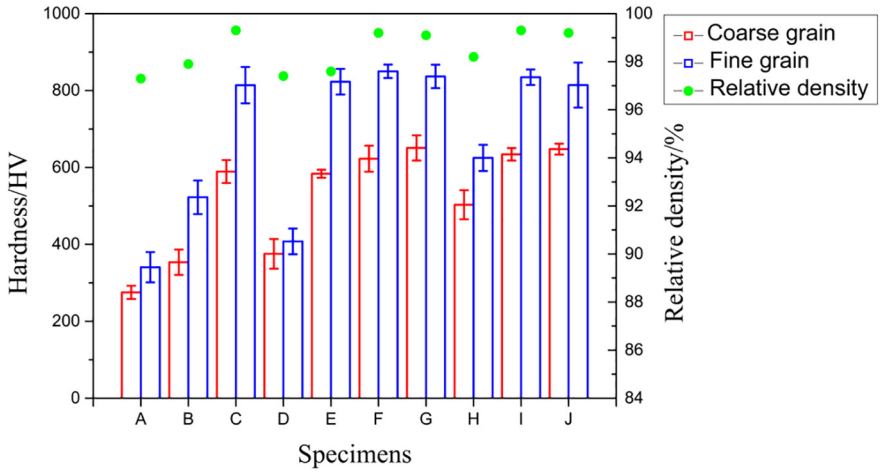

Fig. 8. Surface hardness and relative density of as-sintered samples in various processing conditions. A, B, C and D were milled for 0 h, 24 h, 30 h and 36 h, respectively, pressed at 50 MPa, sintered with heat rate at 100 K/min. E, F and G were milled for 30 h, pressed at 40 MPa, 60 MPa and 80 MPa, respectively, sintered with heat rate at 100 K/min. H, I and J were milled for 30 h, pressed at 60 MPa, sintered with heating rates at 50 K/min, 200 K/min and 400 K/min, respectively.

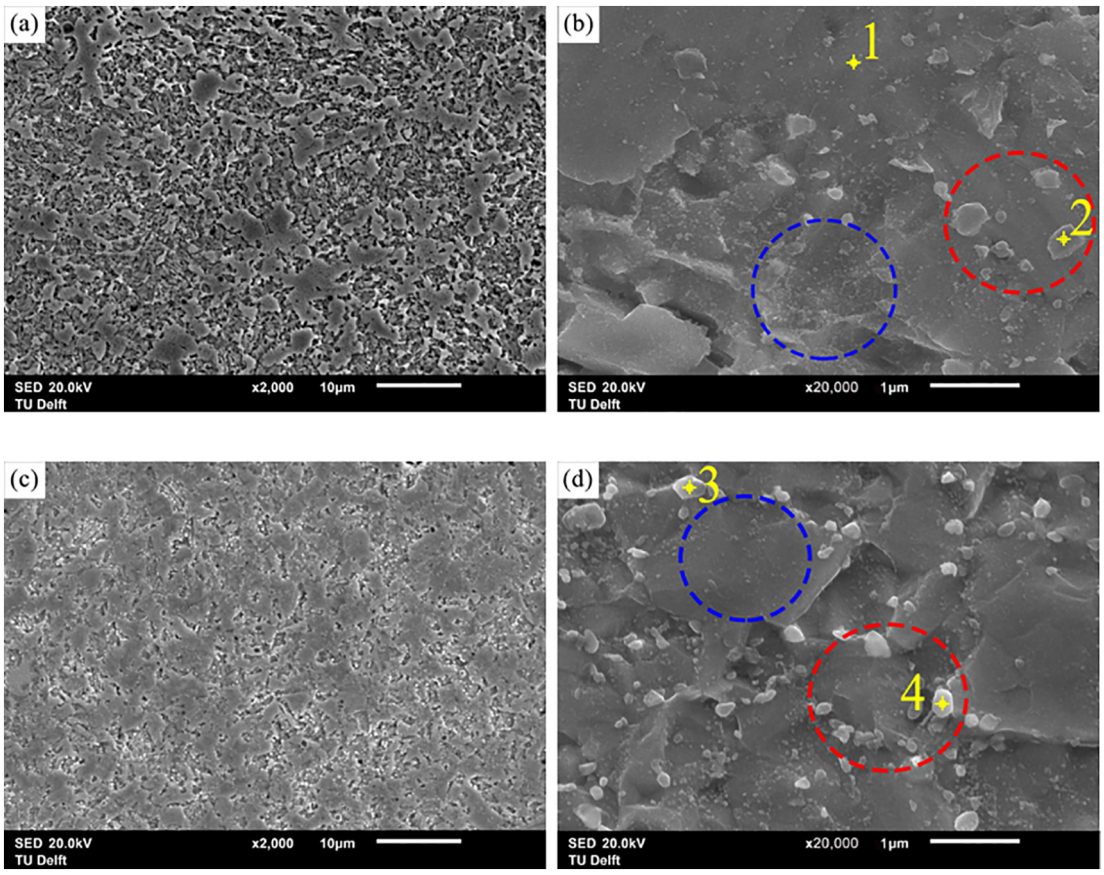

Fig. 9. Morphology of as-produced (a), (b) and heat-treated (c), (d) samples etched with Kalling's 1. The inserted drawings indicate the locations of precipitates.

Also, according to Diouf and Molinari [27], the sintered material "remembers" the size of the starting powder. Smaller particles tend to form smaller grains, leading to a higher density and hardness based on an extrapolation of the Hall-Petch relationship.

From C, E, F and G, it can be seen that the hardness and density of the SPS prepared samples increase with the applied pressure until 60 MPa. The relative density reaches 99.2% considering the theoretical density for ODS Fe—9Cr steels is 7.82 g/cm^3 [28], revealing a highly compacted bulk steel. When the pressure was further increased to 80 MPa, the hardness and density show no significant change, indicating the best possible properties have been obtained. The role of pressure in SPS is not only rearranging the particles and breaking up the agglomerates, but also an extra driving force for densification [17]. With higher pressure applied, the particles are sintered more efficiently, resulting in limited grain growth and less porosity.

The density and surface hardness of samples processed with different heating rates are exhibited in F, H, I and J. A density of 98.0% at the heating rate of 50 K/min shows a limited sintering during SPS. With a heating rate of 100 K/min, the density and surface hardness were significantly increased. This may be due to a higher electric current density passing through the powders, leading to the generation of higher Joule heat and an improved sintering [29]. Further increase of the heating rate above 100 K/min does not have an obvious effect on the final properties.

3.3. Microstructure characterisation

The morphology of as-produced and heat-treated SPS prepared samples was observed by SEM and is shown in Fig. 9. Here the sample F in Fig. 8 with the best properties is taken as an example. It is found that a mixed microstructure with ultrafine grains (UFG, ~200 nm) and coarse grains (CG, ~3 μm) is formed in the as-produced alloy (Fig. 9(a)). This feature can also be described as a core-shell microstructure, where the UFG zone acts as the core and the CG zone acts as the shell. Bimodal grain size distributions were also reported in other studies on ODS steels produced by powder metallurgy [18,30–32]. This microstructure was usually attributed to the milling process: (i) As the precipitates that are nanometre scale Y—O tend to impede grain growth through a Zener-type pinning effect on subgrain boundaries [30], the formation of fine grains is presumably due to the resistance to recovery and growth in the regions with a higher density of nanoprecipitates [31]. (ii) Heterogenous recrystallisation due to unevenly stored energy after milling, causes rapid growth of some grains at the expense of their higher energy neighbours [32]. In some studies, the SPS process was

Table 5
Chemical composition of the points indicated in Fig. 9(b) and (d).

Elements (wt./%)	Cr	W	Mn	Y	V	Ta	C	Fe
Point 1	9.65 ± 0.82	1.01 ± 0.10	0.28 ± 0.10	0.12 ± 0.08	0.05 ± 0.02	0.43 ± 0.06	0.56 ± 0.06	Bal.
Point 2	30.65 ± 0.90	4.38 ± 0.33	–	–	–	–	1.59 ± 0.06	Bal.
Point 3	28.13 ± 0.82	1.69 ± 0.15	–	–	–	0.12 ± 0.12	1.64 ± 0.05	Bal.
Point 4	22.76 ± 0.85	3.54 ± 0.33	0.62 ± 0.12	–	0.14 ± 0.05	0.08 ± 0.08	1.74 ± 0.06	Bal.

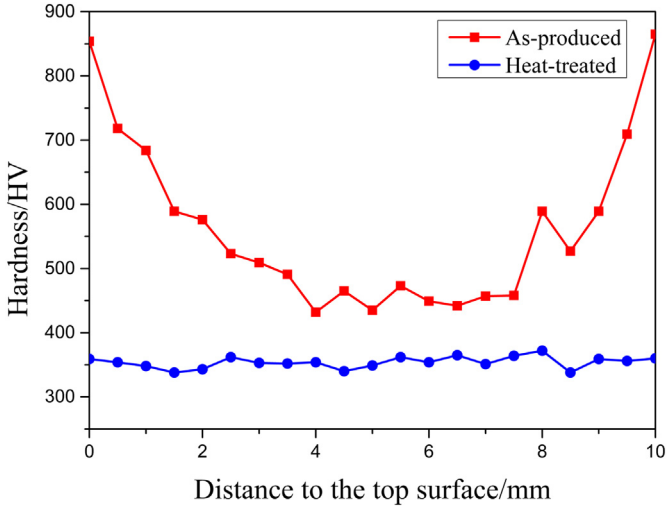

Fig. 10. Vickers hardness profile of the cross section of the as-produced and heat-treated samples.

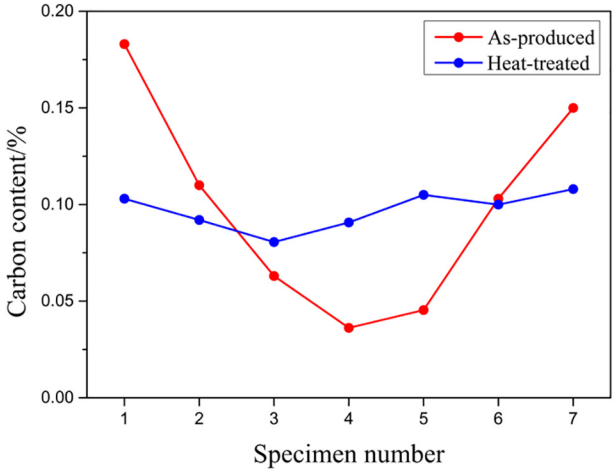

Fig. 12. Carbon content of the tensile specimens.

also seen as one of the causes of the bimodal microstructure [18]. In SPS, electric current passes more easily along the particle surfaces than through the cores due to a lower electrical resistance. The temperature distribution in the powder particles is heterogeneous as the Joule heating is more intensive in the area of sintering necks. The grains in these areas will grow to a larger size due to the higher temperature. Meanwhile, the grains inside the severely deformed powders will recrystallise and form ultrafine grains [33]. All these factors might contribute to the bimodal nature of the microstructure. A bimodal microstructure of UFG surrounded by CG is formed finally.

As indicated in the red circles in Fig. 9(b) and (d), course precipitates with sizes of 50–200 nm were found in the microstructure. The chemical composition of the precipitates was determined by EDS, as shown in Table 5. They are assumed to be $M_{23}C_6$ carbides (M = Fe, Cr, W) based on their size and chemical composition. Note that in the heat-treated sample, these carbides are found to be more preferably located at grain boundaries. The precipitation of $M_{23}C_6$ along grain boundaries in heat-treated steels is a quite common phenomenon, mainly ascribed to the redistribution of solution alloying elements and the decrease in volume free energy [34]. It was observed that a large number of precipitates with sizes around 10 nm in the as-produced and heat-treated alloy, shown in the blue circles. They are assumed to be Y_2O_3, based on their size and density in the matrix.

3.4. Properties investigation

Fig. 10 shows the Vickers hardness profile of a cross section of the as-produced and heat-treated sample F with the maximum value on the top and bottom surfaces and minimum in the centre. This is probably because of the inhomogeneous distribution of carbides in the as-produced sample. The carbon in the graphite mould diffused to some extent into the sample during SPS even though BN spray was used to reduce the diffusion. As a result, the carbon content in the surface is higher than that in the middle of the sample. As the $M_{23}C_6$ carbides have a strong pinning effect on the migration of dislocations and subgrains, the top and bottom surfaces will have a higher hardness.

After annealing at 1423 K for 1 h, air cooling and tempering at 973 K for 1 h, and finally air cooling to room temperature, a more homogenous microstructure through carbon diffusion, carbides dissolution and reprecipitation is obtained. It can be seen that the differences in hardness have been virtually eliminated, indicating a more homogeneous distribution of carbides. Note that the hardness of the heat-treated sample is significantly lower than that of the as-produced sample. This is due to the reduction in the dislocation density by static recovery, grain growth and coarsening of carbides, reducing the strengthening effect stabilizing the laths or subgrains [35]. The pinning effect of Y_2O_3 on the dislocations and grain boundaries has a large contribution to the remaining hardness. The average hardness of the heat-treated sample is 354 HV, very close to that of the ODS Eurofer mentioned in Ref. [36] (about 350 HV), which was produced by MA and HIP followed by a heat treatment of annealing and tempering.

The tensile properties of the as-produced and heat-treated sample F are presented in Fig. 11. Similar to the trend of the hardness profile, we found higher tensile strength and yield strength of as-produced specimen 1 and 7 from Fig. 1(b), resulting from an increased carbon content close to the surface. Combustion analyse were performed to characterise the carbon content of the tensile specimens more accurately. The results are shown in Fig. 12. In the as-produced condition, the carbon content of

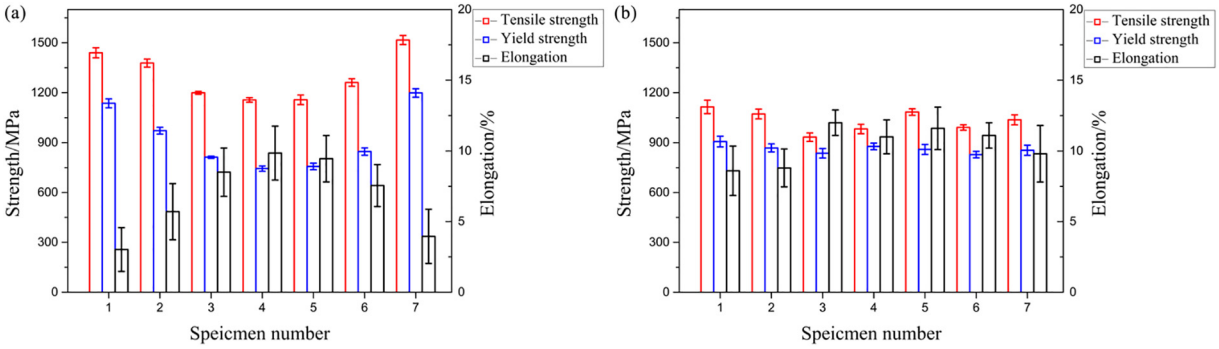

Fig. 11. Ultimate tensile strength, yield strength and elongation of the as-produced (a) and heat-treated (b) samples at the location indicated in Fig. 1(b).

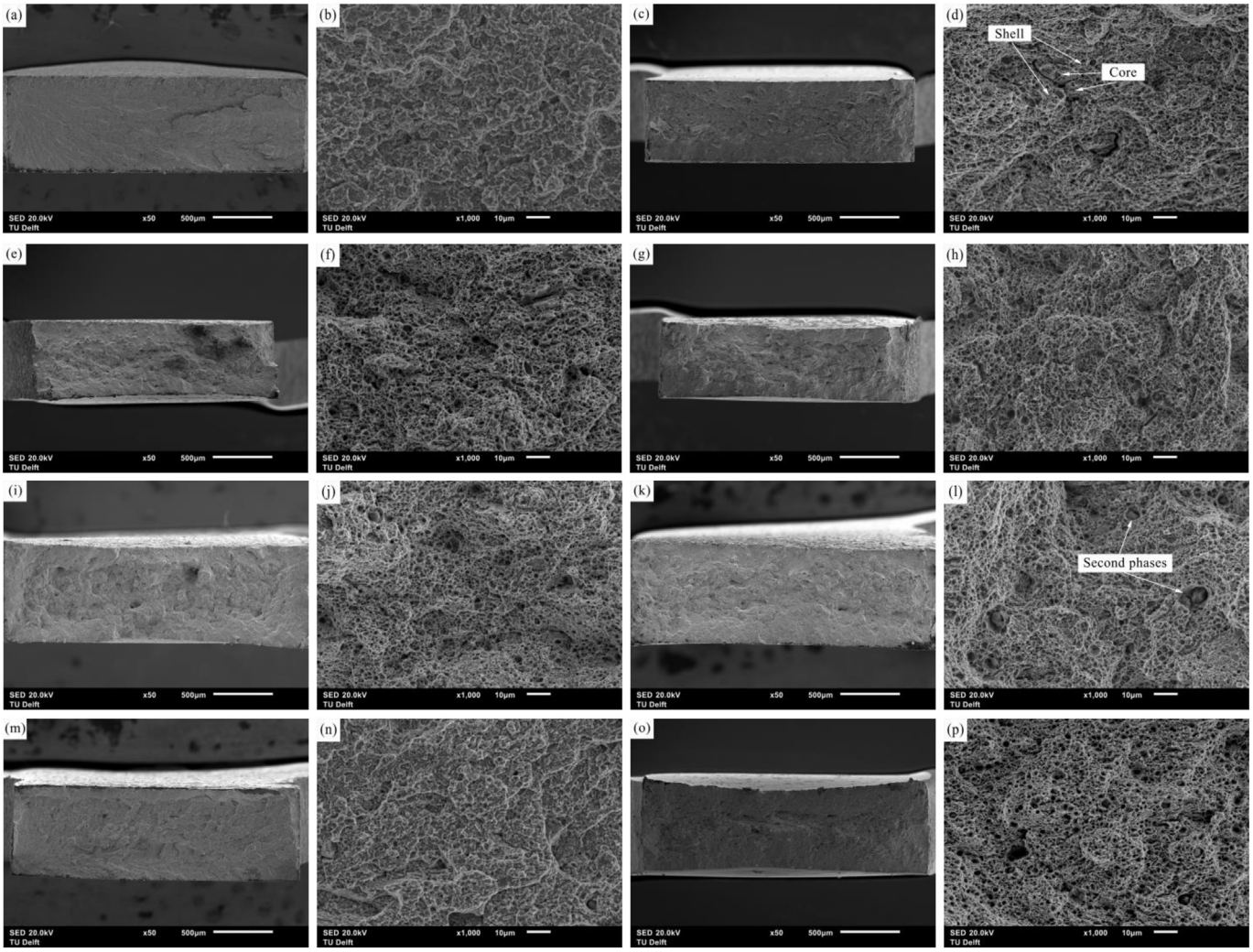

Fig. 13. SEM micrographs of fracture surfaces of SPS prepared samples after tensile test. As-produced sample 1: (a) and (b), sample 2: (c) and (d), sample 3: (e) and (f), sample 4: (g) and (h), sample 5: (i) and (j), sample 6: (k) and (l), sample 7: (m) and (n) and heat-treated sample 3: (o) and (p).

specimen 1 and 7 are 0.18% and 0.15%, respectively, much higher than that of the specimen in the middle, which is 0.04%. A higher content of carbon causes not only a strength increment but also a reduction in elongation, as $M_{23}C_6$ carbides usually act as preferential sites for cavity nucleation due to stress concentration [37]. Reduced ductility and elongation will therefore be obtained before rupture. In contrast, the difference of the carbon content in the heat-treated tensile specimens is much smaller, a more homogenous microstructure and mechanical properties in the steel matrix could be achieved under this condition. The results shown in Fig. 11(b) have confirmed such deduction. Moreover, the strength of the heat-treated samples is decreased, while the elongation is increased after annealing and tempering. This can be explained by the redistribution of carbon atoms, recovery of dislocations and decomposition of brittle martensite during the heat treatment. A more reasonable balance between the strength and ductility has been obtained.

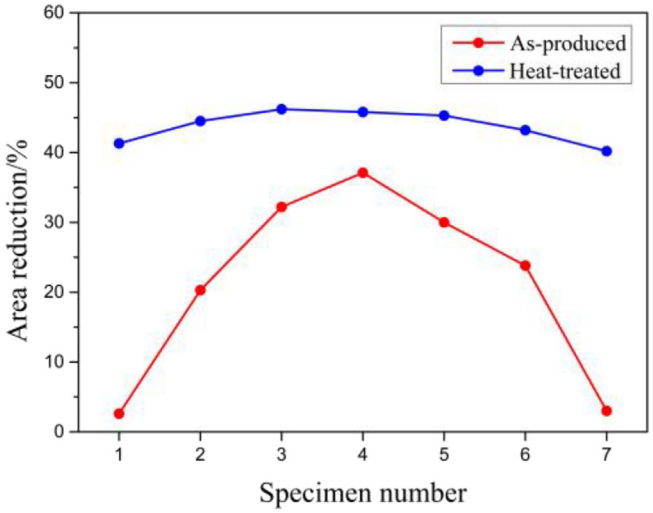

Fig. 14. Area reduction of the as-produced and heat-treated samples.

Fractographic examinations were performed on the fracture surfaces from tensile testing by SEM to understand the failure patterns (Fig. 13). The area reduction of each sample was measured and is presented in Fig. 14. It can be seen that sample 1 and 7 exhibit an intergranular fracture mode. Failure occurred perpendicular to the direction of the tensile force applied, with virtually no necking. The area reduction of sample 1 and 7 are 2.6% and 3.0%, respectively. In contrast, the other samples show a typical ductile fracture mode with numerous dimple features. The area reduction is significantly increased compared to sample 1 and 7. For instance, the area reduction of sample 4 is as high as 37.1%, indicating significant necking and a more ductile fracture. At higher magnification, coarse second phase particles (approximately 8 μm) were observed inside the dimples (Fig. 13(l)). These particles are rich in Fe, Cr, W and C, confirmed by EDS analysis. Second phase particles are known to promote

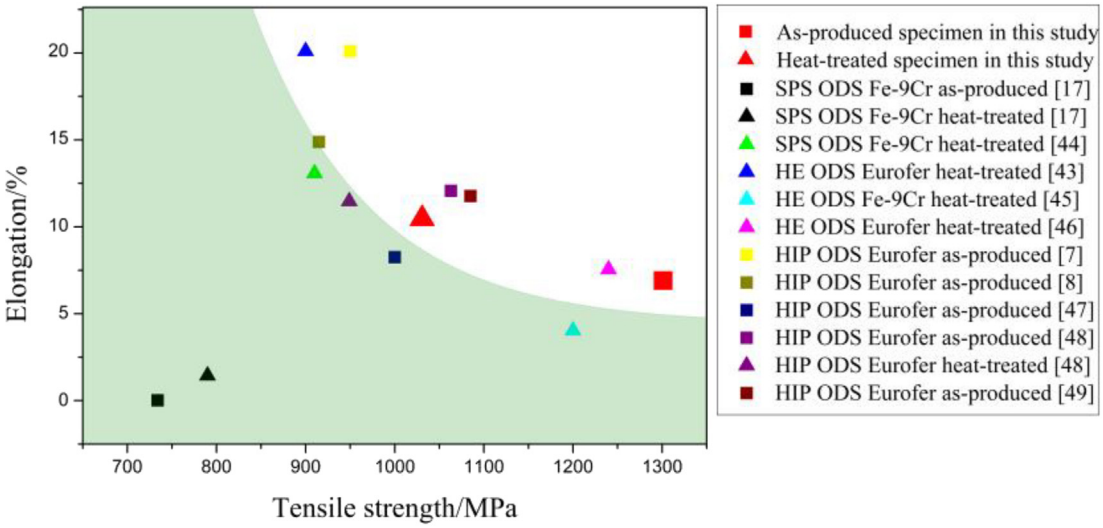

Fig. 15. Elongation versus tensile strength of the as-produced and heat-treated ODS Eurofer compared to those in references [43–49].

void nucleation, growth and coalescence, which facilitate crack initiation and propagation and reduce the ductility. The fracture surface of the heat-treated sample shows larger dimples compared to that of the as-produced samples, showing the benefits of the heat treatment.

It is worth noting that the size and geometry of the dimples observed in the fractures are also bimodal, which can probably be ascribed to the bimodal grain structure. In recent studies, it has been demonstrated that materials having bimodal microstructures yield balance between strength and ductility, where UFG microstructures provide high strength and CG microstructures guarantee enhanced ductility [38–40]. In the early stages of tensile loading, the CG regions experienced yielding prior to the UFG regions. This would cause a slight decrease of the yield strength compared to fully UFG samples. However, due to the high work hardening capacity of the CG material, the strength of the bimodal structure is not significantly weakened [41]. As shown in Fig. 13(d), the cracks initiated more easily at the core/shell interfaces due to stress mismatch. The cracks started to propagate until reaching the ductile shell region with additional plastic deformation, leading to the inhibition or even termination of the crack growth. Consequently, plastic strain accumulates in the core/shell structure and the strain hardening stage is extended before fracture occurs. The ductility of the specimen is therefore improved through this ductile-phase toughing mechanism [42].

Fig. 15 summarizes the elongation as a function of tensile strength of the as-produced and heat-treated ODS Eurofer compared to those reported in references. Results of the ODS Fe—9Cr steel were also collected and compared due to limited range of data available on ODS Eurofer. It can be seen that all of the published results of the SPS-produced steels are on the left side of the Elongation-Tensile strength trend line. The results in this study stand out from the trend line, showing a good combination between high strength and reasonable ductility. From the figure, it is also worth noting that the results of this study are comparable to the HIP and HE prepared ODS Eurofer. Considering the remarkably lower pressure and time needed for consolidation, SPS shows significant potential as a cost-effective technique to produce high performance ODS Eurofer.

4. Conclusions

ODS Eurofer was produced by MA, SPS and subsequent heat treatment. The influence of MA and SPS parameters on the microstructure and mechanical properties was studied in detail. The following conclusions can be drawn:

(1) MA is a necessary step in the process chain to achieve consistent and reproducible microstructures of ODS Eurofer. After 30 h of milling, the powders have a minimum average size (approximately 10.7 μm) and a homogeneous chemical composition. ODS Eurofer shows the highest density and microhardness when milled for 30 h, sintered at 1373 K with a heating rate of 100 K/ min at a pressure of 60 MPa.

(2) The morphology of SPS prepared ODS Eurofer displays a bimodal microstructure with coarse grains and ultrafine grains. Coarse $M_{23}C_6$ carbides are found to decorate the grain boundaries; nanosized Y_2O_3 are homogenously dispersed in the steel matrix.

(3) The top and bottom surfaces of the as-produced sample present a higher microhardness and tensile strength associate with higher carbon content. The heat-treated ODS Eurofer exhibits a good combination of high strength and reasonable ductility. Fracture analysis shows a ductile failure with well-defined dimples. SPS has shown advantages as a cost-effective consolidation approach to produce ODS Eurofer with comparable quality to HIP and HE at significantly lower pressures and times.

CRediT authorship contribution statement

J. Fu: Conceptualization, Investigation, Methodology, Validation, Writing - original draft, Writing - review & editing, Visualization. **J.C. Brouwer:** Investigation, Methodology, Software. **I.M. Richardson:** Conceptualization, Methodology, Writing - review & editing, Supervision, Project administration, Funding acquisition. **M.J.M. Hermans:** Conceptualization, Methodology, Validation, Writing - review & editing, Visualization, Supervision, Project administration, Funding acquisition.

Acknowledgements

This research was carried out under project number T16010f in the framework of the Partnership Program of the Materials innovation institute M2i (www.m2i.nl) and the Netherlands Organisation for Scientific Research (www.nwo.nl). The authors thank the industrial partner Nuclear Research and Consultancy Group (NRG) in this project for the financial support. The authors also thank Ruud Hendrikx for the XRD analysis and Prof. Dr. ir. Wim Sloof for the contribution in the SEM analysis.

Data availability

The raw/processed data required to reproduce these findings cannot be shared at this time as the data also forms part of an ongoing study.

References

[1] T. Gräning, M. Rieth, J. Hoffmann, A. Möslang, Production, microstructure and mechanical properties of two different austenitic ODS steels, J. Nucl. Mater. 487 (2017) 348–361.
[2] Y. Yano, T. Tanno, H. Oka, S. Ohtsuka, T. Inoue, S. Kato, T. Furukawa, T. Uwaba, T. Kaito, S. Ukai, Ultra-high temperature tensile properties of ODS steel claddings under severe accident conditions, J. Nucl. Mater. 487 (2017) 229–237.
[3] L. Zhang, L. Yu, Y. Liu, C. Liu, H. Li, J. Wu, Influence of Zr addition on the microstructures and mechanical properties of 14Cr ODS steels, Mater. Sci. Eng. A 695 (2017) 66–73.
[4] R. Lindau, A. Möslang, M. Rieth, M. Klimiankou, E. Materna-Morris, A. Alamo, A.-A. Tavassoli, C. Cayron, A.-M. Lancha, P. Fernandez, Present development status of EUROFER and ODS-EUROFER for application in blanket concepts, Fusion Eng. Des. 75 (2005) 989–996.
[5] H. Dong, L. Yu, Y. Liu, C. Liu, H. Li, J. Wu, Effect of hafnium addition on the microstructure and tensile properties of aluminum added high-Cr ODS steels, J. Alloys Compd. 702 (2017) 538–545.
[6] M. Klimenkov, R. Lindau, U. Jäntsch, A. Möslang, Effect of irradiation temperature on microstructure of ferritic-martensitic ODS steel, J. Nucl. Mater. 493 (2017) 426–435.
[7] R. Lindau, A. Möslang, M. Schirra, P. Schlossmacher, M. Klimenkov, Mechanical and microstructural properties of a hipped RAFM ODS-steel, J. Nucl. Mater. 307 (2002) 769–772.
[8] R. Schaeublin, T. Leguey, P. Spätig, N. Baluc, M. Victoria, Microstructure and mechanical properties of two ODS ferritic/martensitic steels, J. Nucl. Mater. 307 (2002) 778–782.
[9] J. Shen, H. Yang, Y. Li, S. Kano, Y. Matsukawa, Y. Satoh, H. Abe, Microstructural stability of an as-fabricated 12Cr-ODS steel under elevated-temperature annealing, J. Alloys Compd. 695 (2017) 1946–1955.
[10] R. Gao, B. Cheng, L. Zeng, S. Miao, J. Hou, T. Zhang, X. Wang, Q. Fang, C. Liu, Microstructure, hardness and defect structure of the He irradiated ODS ferritic steel, J. Alloys Compd. 691 (2017) 653–658.
[11] P. Miao, G. Odette, T. Yamamoto, M. Alinger, D. Hoelzer, D. Gragg, Effects of consolidation temperature, strength and microstructure on fracture toughness of nanostructured ferritic alloys, J. Nucl. Mater. 367 (2007) 208–212.
[12] Y. Li, J. Shen, F. Li, H. Yang, S. Kano, Y. Matsukawa, Y. Satoh, H. Fu, H. Abe, T. Muroga, Effects of fabrication processing on the microstructure and mechanical properties of oxide dispersion strengthening steels, Mater. Sci. Eng. A 654 (2016) 203–212.
[13] O. Guillon, J. Gonzalez-Julian, B. Dargatz, T. Kessel, G. Schierning, J. Räthel, M. Herrmann, Field-assisted sintering technology/spark plasma sintering: mechanisms, materials, and technology developments, Adv. Eng. Mater. 16 (2014) 830–849.
[14] M. Suárez, A. Fernández-Camacho, J.L. Menéndez, R. Torrecillas, Challenges and Opportunities for Spark Plasma Sintering: A Key Technology for a New Generation of Materials, InTech, 2013.
[15] C. Zhang, A. Kimura, R. Kasada, J. Jang, H. Kishimoto, Y. Yang, Characterization of the oxide particles in Al-added high-Cr ODS ferritic steels, J. Nucl. Mater. 417 (2011) 221–224.
[16] Z. Munir, U. Anselmi-Tamburini, M. Ohyanagi, The effect of electric field and pressure on the synthesis and consolidation of materials: a review of the spark plasma sintering method, J. Mater. Sci. 41 (2006) 763–777.
[17] Q. Sun, Y. Zhou, Q. Fang, R. Gao, T. Zhang, X. Wang, Development of 9Cr-ODS ferritic–martensitic steel prepared by chemical reduction and mechanical milling, J. Alloys Compd. 598 (2014) 243–247.
[18] R. Xie, Z. Lu, C. Lu, Z. Li, X. Ding, C. Liu, Microstructures and mechanical properties of 9Cr oxide dispersion strengthened steel produced by spark plasma sintering, Fusion Eng. Des. 115 (2017) 67–73.
[19] S. Ukai, Microstructure and high-temperature strength of 9CrODS ferritic steel, Metal, Ceramic and Polymeric Composites for Various Uses, InTech, 2011.
[20] C. Suryanarayana, Mechanical alloying and milling, Prog. Mater. Sci. 46 (2001) 1–184.
[21] G. Williamson, W. Hall, X-ray line broadening from filed aluminium and wolfram, Acta Metall. 1 (1953) 22–31.
[22] Y. Kimura, S. Takaki, S. Suejima, R. Uemori, H. Tamehiro, Ultra grain refining and decomposition of oxide during super-heavy deformation in oxide dispersion ferritic stainless steel powder, ISIJ Int. 39 (1999) 176–182.
[23] P.-Y. Lee, J.-L. Yang, H.-M. Lin, Amorphization behaviour in mechanically alloyed Ni-Ta powders, J. Mater. Sci. 33 (1998) 235–239.
[24] A. Ramar, Z. Oksiuta, N. Baluc, R. Schäublin, Effect of mechanical alloying on the mechanical and microstructural properties of ODS EUROFER 97, Fusion Eng. Des. 82 (2007) 2543–2549.
[25] A. Pandey, K. Jayasankar, P. Parida, M. Debata, B. Mishra, S. Saroja, Optimization of milling parameters, processing and characterization of nano-crystalline oxide dispersion strengthened ferritic steel, Powder Technol. 262 (2014) 162–169.
[26] H. Abelson, The creation of OpenCourseWare at MIT, J. Sci. Educ. Technol. 17 (2008) 164–174.
[27] S. Diouf, A. Molinari, Densification mechanisms in spark plasma sintering: effect of particle size and pressure, Powder Technol. 221 (2012) 220–227.
[28] M.A. Auger, V. De Castro, T. Leguey, A. Muñoz, R. Pareja, Microstructure and mechanical behavior of ODS and non-ODS Fe-14Cr model alloys produced by spark plasma sintering, J. Nucl. Mater. 436 (2013) 68–75.
[29] M. Staltsov, I. Chernov, I. Bogachev, B. Kalin, E. Olevsky, L. Lebedeva, A. Nikitina, Optimization of mechanical alloying and spark-plasma sintering regimes to obtain ferrite-martensitic ODS steel, Nucl. Mater. Energy 9 (2016) 360–366.
[30] K.D. Zilnyk, H.R.Z. Sandim, R.E. Bolmaro, R. Lindau, A. Möslang, A. Kostka, D. Raabe, Long-term microstructural stability of oxide-dispersion strengthened Eurofer steel annealed at 800 °C, J. Nucl. Mater. 448 (2014) 33–42.
[31] H. Kishimoto, M.J. Alinger, G.R. Odette, T. Yamamoto, TEM examination of microstructural evolution during processing of 14CrYWTi nanostructured ferritic alloys, J. Nucl. Mater. 329-333 (2004) 369–371.
[32] X. Boulnat, M. Perez, D. Fabregue, T. Douillard, M.H. Mathon, Y.D. Carlan, Microstructure evolution in nano-reinforced ferritic steel processed by mechanical alloying and spark plasma sintering, Metall. Mater. Trans. A 45 (2014) 1485–1497.
[33] G. Ji, N. Bozzolo, T. Grosdidier, S. Launois, The mechanisms of microstructure formation in a nanostructured oxide dispersion strengthened FeAl alloy obtained by spark plasma sintering, Intermetallics 15 (2007) 108–118.
[34] L. Zheng, X. Hu, X. Kang, D. Li, Precipitation of $M_{23}C_6$ and its effect on tensile properties of 0.3C-20Cr-11Mn-1Mo-0.35N steel, Mater. Des. 78 (2015) 42–50.
[35] M. Pérez, Impact of annealing treatments on the softening and work hardening behaviour of Jethete M152 alloy for subsequent cold forming processes, Mater. Sci. Eng. A 690 (2017) 303–312.
[36] R.A. Renzetti, H.R.Z. Sandim, M.J.R. Sandim, A.D. Santos, A. Möslang, D. Raabe, Annealing effects on microstructure and coercive field of ferritic-martensitic ODS Eurofer steel, Mater. Sci. Eng. A 528 (2011) 1442–1447.
[37] H.U. Hong, B.S. Rho, S.W. Nam, Correlation of the $M_{23}C_6$ precipitation morphology with grain boundary characteristics in austenitic stainless steel, Mater. Sci. Eng. A 318 (2001) 285–292.
[38] D. Zhao, L. Yong, L. Feng, Y. Wen, L. Zhang, Y. Dou, ODS ferritic steel engineered with bimodal grain size for high strength and ductility, Mater. Lett. 65 (2011) 1672–1674.
[39] G. Dirras, J. Gubicza, S. Ramtani, Q.H. Bui, T. Szilágyi, Microstructure and mechanical characteristics of bulk polycrystalline Ni consolidated from blends of powders with different particle size, Mater. Sci. Eng. A 527 (2010) 1206–1214.
[40] Z. Zhang, S.K. Vajpai, D. Orlov, K. Ameyama, Improvement of mechanical properties in SUS304L steel through the control of bimodal microstructure characteristics, Mater. Sci. Eng. A 598 (2014) 106–113.
[41] J.G. Sevillano, J. Aldazabal, Ductilization of nanocrystalline materials for structural applications, Scr. Mater. 51 (2004) 795–800.
[42] Z. Lee, V. Radmilovic, B. Ahn, E.J. Lavernia, S.R. Nutt, Tensile deformation and fracture mechanism of bulk bimodal ultrafine-grained Al-Mg alloy, Metall. Mater. Trans. A 41 (2010) 795–801.
[43] P. Olier, A. Bougault, A. Alamo, Y. De Carlan, Effects of the forming processes and Y_2O_3 content on ODS-Eurofer mechanical properties, J. Nucl. Mater. 386 (2009) 561–563.
[44] X. Zhou, Y. Liu, L. Yu, Z. Ma, Q. Guo, Y. Huang, H. Li, Microstructure characteristic and mechanical property of transformable 9Cr-ODS steel fabricated by spark plasma sintering, Mater. Des. 132 (2017) 158–169.
[45] S. Ukai, S. Mizuta, M. Fujiwara, T. Okuda, T. Kobayashi, Development of 9Cr-ODS martensitic steel claddings for fuel pins by means of ferrite to austenite phase transformation, J. Nucl. Sci. Technol. 39 (2002) 778–788.
[46] Y. Li, T. Nagasaka, T. Muroga, A. Kimura, S. Ukai, High-temperature mechanical properties and microstructure of 9Cr oxide dispersion strengthened steel compared with RAFMs, Fusion Eng. Des. 86 (2011) 2495–2499.
[47] E. Lucon, Mechanical tests on two batches of oxide dispersion strengthened RAFM steel (EUROFER97), Fusion Eng. Des. 61 (2002) 683–689.
[48] C. Cayron, E. Rath, I. Chu, S. Launois, Microstructural evolution of Y_2O_3 and $MgAl_2O_4$ ODS EUROFER steels during their elaboration by mechanical milling and hot isostatic pressing, J. Nucl. Mater. 335 (2004) 83–102.
[49] D.A. McClintock, M.A. Sokolov, D.T. Hoelzer, R.K. Nanstad, Mechanical properties of irradiated ODS-EUROFER and nanocluster strengthened 14YWT, J. Nucl. Mater. 392 (2009) 353–359.